

Hybrid Active Disturbance Rejection Decoupling Control for Six-Pole Active Magnetic Bearing Based on Improved Genetic Algorithm

Yeming Li and Huangqiu Zhu*

Abstract—For the sake of decoupling the six-pole radial active magnetic bearing (AMB) with mutual coupling of two degrees of freedom, nonlinear and unstable disturbance, a hybrid active disturbance rejection control strategy based on improved genetic algorithm (HADRC-IGA) is proposed. Firstly, the configuration, magnetic circuit and suspension force model of the six-pole radial AMB are explained and established. Secondly, the HADRC-IGA is designed which is improved on the linear active disturbance rejection control (LADRC). Thirdly, the simulation is carried out, which shows that the capacity of resisting disturbance and the decoupling efficiency of two degrees of freedom of the HADRC-IGA are better than that of conventional LADRC. Finally, the experimental platform is constructed, and the experiments are conducted, which verify the performance of the proposed decoupled control system.

1. INTRODUCTION

As a supporting part of mechanical equipment, bearing is one of the important factors for the normal operation of the mechanical equipment in industry, agriculture, and transportation. It is difficult to achieve the rapid rotation of the traditional bearing shaft due to the friction of the rotor. The traditional rolling bearing causes the rotating speed of the shaft to be low because of the friction of the rotor. Over time, new bearings such as aerostatic bearings, liquid dynamic bearings, and magnetic bearings are proposed to apply in scientific manufacturing [1–3]. A three-pole radial active magnetic bearing (AMB) is developed, which allows the rotor to be stably suspended in space, without making mechanical contact with the stator. It has the excellent characteristics of low vibration, lubrication-free, frictionless, high speed, and high precision [4–6]. At present, three-pole radial AMB has been used in aerospace, compressors, and turbomolecular pumps [7, 8]. In order to overcome the disadvantage of a strong coupling between the control current and suspension force due to the structural asymmetry, and to reduce the volume and cost of magnetic bearings, a six-pole radial AMB is proposed, which implements a structural symmetry.

However, the six-pole radial AMB solves the coupling problem due to the imbalance magnetic path, and it still has the displacement coupling in the displacement two-degrees of freedom, which hinders the stable operation of high precision of the six-pole radial AMB [9]. For the coupling problem between the x - and y -direction displacements of magnetic bearings, a variety of vibration compensation methods are put forward. In [10], a modal decoupling control is designed to decouple the radial translations modal and tilting modal of the rotor of the active magnetic bearing. However, the method does not realize the displacement coupling in the two directions of the AMB. In [11], a variable reconstruction method is proposed to convert the multi-input multi-output AMB into a single-input single-output system. However, this scheme is limited by the uncertainty of the model parameters and is difficult to

Received 15 September 2022, Accepted 5 December 2022, Scheduled 9 December 2022

* Corresponding author: Huangqiu Zhu (zhuhuangqiu@ujs.edu.cn).

The authors are with the School of Electrical and Information Engineering, Jiangsu University, Zhenjiang 212013, China.

implement. In [12], a neural network generalized inverse control is proposed which realizes the decoupling between x direction displacement and y direction displacement of the five degrees of freedom magnetic bearing, but it has high requirements for the training sample data, which is not easy to realize.

A linear active disturbance rejection control method (LADRC) is proposed to decouple the magnetic bearings in [13]. The LADRC has the characteristics of decoupling the rotor system without establishing the accurate mathematical model of the magnetic bearings [14, 15].

In this paper, a hybrid active disturbance rejection controller based on improved genetic algorithm (HADRC-IGA) is proposed to decouple the six-pole radial AMB driven by the inverter. At first, a model compensation strategy is used to set the parameters of LADRC. Then, the hybrid active disturbance rejection control combining the advantages of the linear extended state observer (LESO) and nonlinear state error feedback control law (NLSEF) is designed. Next, an improved genetic algorithm which avoids falling into the local optima is proposed, and the parameters of the NLSEF are adjusted by using the improved genetic algorithm. Finally, the high efficiency of the HADRC-IGA is demonstrated through the simulations and experiments.

2. STRUCTURE DESIGN AND SUSPENSION FORCE MODEL OF THE SIX-POLE RADIAL AMB

2.1. Structure Design of the Six-Pole Radial AMB

The structure and magnetic circuit of the six-pole radial AMB are shown in Fig. 1. The six-pole radial AMB includes a radial control coil, rotor, rotating shaft, and radial stator. Among them, the rotor and radial stator are made of silicon steel stack, and the rotor coaxial sleeve is located outside the shaft. The rotor has external radial magnetic poles and radial control coils. There are 6 radial magnetic poles around the radial control coil, which are star connected as the radial coil and winding direction of a phase.

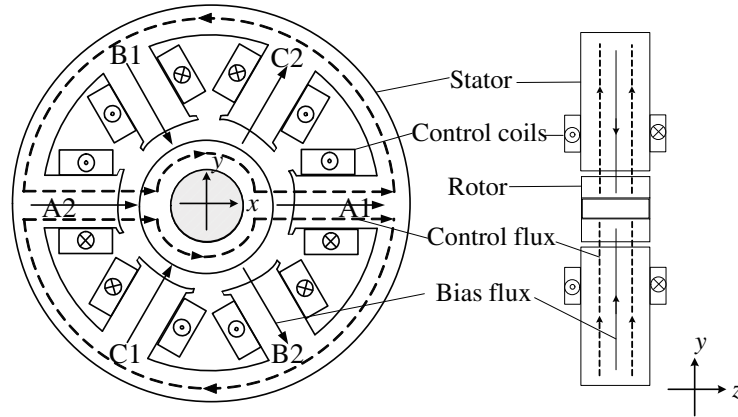


Figure 1. Structure and magnetic circuit of the six-pole radial AMB.

2.2. Suspension Force Model of the Six-Pole Radial AMB

The equivalent magnetic circuit diagram is shown in Fig. 2. N is the number of turns of radial coils; Ni_j ($j = A, B, C$) is the ampere turns of the control coil; i_A, i_B, i_C are the control currents; Φ_{j1}, Φ_{j2} ($j = A, B, C$) are the synthetic magnetic flux in the corresponding air gap.

As shown in Fig. 2, G_{j1}, G_{j2} ($j = A, B, C$) are the magnetic reluctance of radial air gap, which

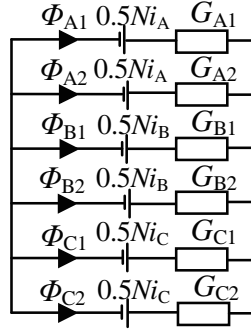


Figure 2. Equivalent magnetic circuit diagram of six-pole radial AMB.

are expressed as:

$$\begin{cases} G_{A1} = \frac{\mu_0 S_r}{\delta_r - x}, & G_{A2} = \frac{\mu_0 S_r}{\delta_r + x} \\ G_{B1} = \frac{\mu_0 S_r}{\delta_r + x/2 - \sqrt{3}y/2}, & G_{B2} = \frac{\mu_0 S_r}{\delta_r - x/2 + \sqrt{3}y/2} \\ G_{C1} = \frac{\mu_0 S_r}{\delta_r + x/2 + \sqrt{3}y/2}, & G_{C2} = \frac{\mu_0 S_r}{\delta_r - x/2 - \sqrt{3}y/2} \end{cases} \quad (1)$$

where x and y denote the actual displacement from the symmetry axis; δ_r is the length of the radial air gap; μ is the vacuum permeability; S_r is the magnetic pole area.

Based on the Kirchhoff's law, the magnetic flux produced by the radial coil at each gap can be expressed as follows:

$$\begin{cases} \Phi_{A1} = \frac{(G_{B1} + G_{B2} + G_{C1} + G_{C2})i_A - (G_{B1} + G_{B2})i_B - (G_{C1} + G_{C2})i_C}{2(G_{A1} + G_{A2} + G_{B1} + G_{B2} + G_{C1} + G_{C2})} N G_{A1} \\ \Phi_{A2} = \frac{(G_{B1} + G_{B2} + G_{C1} + G_{C2})i_A - (G_{B1} + G_{B2})i_B - (G_{C1} + G_{C2})i_C}{2(G_{A1} + G_{A2} + G_{B1} + G_{B2} + G_{C1} + G_{C2})} N G_{A2} \\ \Phi_{B1} = \frac{(G_{A1} + G_{A2} + G_{C1} + G_{C2})i_B - (G_{A1} + G_{A2})i_A - (G_{C1} + G_{C2})i_C}{2(G_{A1} + G_{A2} + G_{B1} + G_{B2} + G_{C1} + G_{C2})} N G_{B1} \\ \Phi_{B2} = \frac{(G_{A1} + G_{A2} + G_{C1} + G_{C2})i_B - (G_{A1} + G_{A2})i_A - (G_{C1} + G_{C2})i_C}{2(G_{A1} + G_{A2} + G_{B1} + G_{B2} + G_{C1} + G_{C2})} N G_{B2} \\ \Phi_{C1} = \frac{(G_{A1} + G_{A2} + G_{B1} + G_{B2})i_C - (G_{A1} + G_{A2})i_A - (G_{B1} + G_{B2})i_B}{2(G_{A1} + G_{A2} + G_{B1} + G_{B2} + G_{C1} + G_{C2})} N G_{C1} \\ \Phi_{C2} = \frac{(G_{A1} + G_{A2} + G_{B1} + G_{B2})i_C - (G_{A1} + G_{A2})i_A - (G_{B1} + G_{B2})i_B}{2(G_{A1} + G_{A2} + G_{B1} + G_{B2} + G_{C1} + G_{C2})} N G_{C2} \end{cases} \quad (2)$$

According to the suspension force and magnetic flux relation, the suspension force generated by each radial magnetic pole can be obtained as:

$$F_i = \frac{\Phi_i^2}{2\mu_0 S_r} \quad (i = A1, A2, B1, B2, C1, C2) \quad (3)$$

After neglecting the infinitesimal quantity above the second order, the suspension forces are projected in the x - and y -directions:

$$\begin{cases} F_x = k_{ir} \cdot i_x + k_r \cdot x \\ F_y = k_{ir} \cdot i_y + k_r \cdot y \end{cases} \quad (4)$$

where $k_{ir} = \frac{\sqrt{3}}{2} \cdot \frac{5S_r\mu_0 N^2 I^2}{24\delta_r^2}$, $k_r = \frac{5S_r\mu_0 N^2 I^2}{24\delta_r^3}$, k_r is the displacement stiffness coefficient, and k_{ir} is the current stiffness coefficient. F_x and F_y are the suspension forces in the x - and y -directions, respectively;

I refers to the bias current connected to each phase coil; i_x and i_y are the two-phase control currents; x and y are the displacements in radial direction.

As can be seen from Eq. (4), the suspension force of the x - and y -directions near the equilibrium position has linear distribution with the control current and displacement in the corresponding direction, respectively.

According to the rotor dynamics theory, the equation of motion of the six-pole radial AMB can be obtained as follows:

$$\begin{cases} m\ddot{x} = F_x \\ m\ddot{y} = F_y - mg \\ J_x\ddot{\theta}_x = -l_a F_y - J_z\Omega\dot{\theta}_y \\ J_y\ddot{\theta}_y = l_a F_x + J_z\Omega\dot{\theta}_x \end{cases} \quad (5)$$

where m is the mass of rotor; g is the gravity constant; Ω is the mechanical angular velocity around the z -axis. J_x , J_y , and J_z are the moment of inertia around the x -, y -, and z -axes, respectively. $J_x = J_y = J_d$. l_a is the distance from the magnetic bearing to the center of mass. θ_x and θ_y are the rotation angles of the rotor around the x - and y -axes, respectively.

The state equation of the six-pole radial AMB can be obtained as follows:

$$\begin{cases} \ddot{x} = \frac{k_x}{m} \left(1 + \frac{ml_a^2}{J_d}\right) x + \frac{k_{i_x}}{m} \left(1 + \frac{ml_a^2}{J_d}\right) i_x - \frac{J_z\Omega}{J_d} \dot{y} \\ \ddot{y} = \frac{k_y}{m} \left(1 + \frac{ml_a^2}{J_d}\right) y + \frac{k_{i_y}}{m} \left(1 + \frac{ml_a^2}{J_d}\right) i_y + \frac{J_z\Omega}{J_d} \dot{x} - g \end{cases} \quad (6)$$

From Eq. (6), the rotor has a displacement coupling in x - and y -directions, so a decoupling control method is necessary.

3. HYBRID ACTIVE DISTURBANCE REJECTION CONTROLLER BASED ON IMPROVED GENETIC ALGORITHM

3.1. Design of the LADRC Based on the Model Compensation

According to Eq. (5), the six-pole radial AMB has strong nonlinear and high coupling properties, which is susceptible to some external factors in the process of operation, which is difficult to accurately control it. To make the rotor run stably, the selection of suitable magnetic bearing controller becomes the key.

LADRC is a new controller. The significance of the linear expansion state observer (LESO) is to estimate each variable and the sum of the disturbances of the controlled subject according to the system output. The function of linear state error feedback (LSEF) is to combine the state variable feedback studied by ESO, so as to obtain the control signal quantity.

The second-order LADRC expression is shown below:

$$\begin{cases} e(t) = v(t) - z_1(t) \\ \dot{z}_1(t) = z_2(t) - \beta_1 e(t) \\ \dot{z}_2(t) = z_3(t) - \beta_2 e(t) + bu(t) \\ \dot{z}_3 = -\beta_3 e(t) \\ u_0(t) = k_p e(t) - k_d z_2(t) \\ u(t) = u_0(t) - z_3(t)/b \end{cases} \quad (7)$$

The method of setting parameters of LESO by bandwidth is given in [16]. Parameters β_1 , β_2 , and β_3 can be configured as $3\omega_0$, $3\omega_0^2$, and ω_0^3 . k_p and k_d can be configured as ω_c^2 and $2\omega_c$, where ω_0 is the observer bandwidth, and ω_c is the controller bandwidth [17]. Therefore, the parameters which need to be set in LADRC are only ω_0 , ω_c , and b .

Since all information of the model can be observed and compensated by LESO, LADRC is a control strategy that can achieve better dynamic performance without relying on model information. Without model assistance, the unknown total disturbance includes all external disturbances, control

gain, and the amount of change influenced by uncertainty factors, which all rely on LESO observation and compensation. In view of the above issues, if a part of the model information of the six-pole radial AMB can be obtained through system identification, the uncertainties of the six-pole radial AMB can be compensated, and the observation pressure of LESO can be relieved. Therefore, a model compensation LADRC controller scheme is proposed in this paper for the six-pole radial AMB, which makes full use of the known information of the six-pole radial AMB and adds it to the control strategy of LADRC, so as to improve the control efficiency.

The state equation of the rotor in the x direction can be described as:

$$\begin{cases} \dot{x}_1(t) = x_2(t) \\ \dot{x}_2(t) = f_0(x_1(t), x_2(t)) + \omega(t) + bu(t) \\ y(t) = x_1(t) \end{cases} \quad (8)$$

where $u(t)$ is the control current of the system; $x_1(t)$ is the output signal, in the system is the rotor displacement; $f_0(x_1(t), x_2(t))$ is the internal disturbance of the six-pole radial AMB; $\omega(t)$ is the external disturbance of the system; $\omega(t)$ is unknown; and b is the control gain of the six-pole radial AMB.

Equations (6) and (8) can be combined to obtain:

$$b = \frac{k_{ix}}{m} \left(1 + \frac{ml_a^2}{J_d} \right) \quad (9)$$

According to the principle of model compensation LADRC, the parameter b in LADRC can be set through model information of the six-pole radial AMB.

In summary, the parameters in LADRC are only ω_0 and ω_c . In this paper, ω_0 can be defined as 70 rad/s, and ω_c can be defined as 50 rad/s.

3.2. Design of a Hybrid ADRC

LADRC has fewer parameters and simple tuning due to the LESO and LSEF, but in comparison to nonlinear feedback its efficiency is lower, and its tracking accuracy and response speed are relatively low. As shown in Fig. 3, the LSEF is replaced by the nonlinear state error feedback control law (NLSEF) to constitute a hybrid ADRC (HADRC).

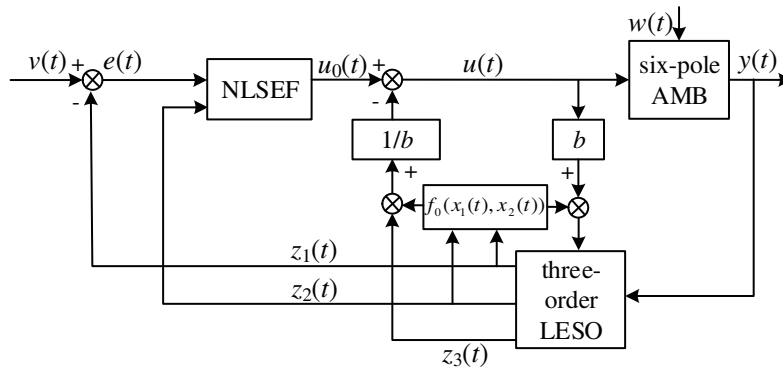


Figure 3. The diagram of HADRC.

The expression of the NLSEF is:

$$u_0(t) = k_p fal(e(t), \alpha_1, \delta) + k_d fal(-z_2(t), \alpha_2, \delta) \quad (10)$$

where the expression of the function fal is:

$$fal(e, \alpha, \delta) = \begin{cases} \frac{e}{\delta^{1-\alpha}}, & |e| \leq \delta \\ |e|^\alpha sgn(e), & |e| > \delta \end{cases} \quad (11)$$

where the function fal is a nonlinear function in the NLSEF; α_1 , α_2 , and δ are adjustable parameters.

When tracking the signal with noise, NLSEF not only has a good effect of filtering noise, but also can quickly track the original signal. When the signal error is large, the function fal produces a smaller feedback gain, and when the error is small, it produces a larger feedback gain, which improves the control characteristics of the system, makes the system have strong robustness and adaptability, and better meets the requirements of system stability and rapidity.

After using the nonlinear function fal , the values of k_p and k_d originally set based on the bandwidth method need to be adjusted. In general, α_1 , α_2 , and δ in the function fal are a set of fixed parameters. In this paper, $\alpha_1 = \alpha_2 = 0.25$, $\delta = 0.05$.

3.3. Improved Genetic Algorithm to Optimize Parameters

The parameters k_p and k_d in NLSEF have a great influence on the capacity of resisting disturbance of the six-pole radial AMB. An improved genetic algorithm (IGA) is proposed which overcomes the local optimization in traditional genetic algorithm, and the specific flowchart is shown in Fig. 4.

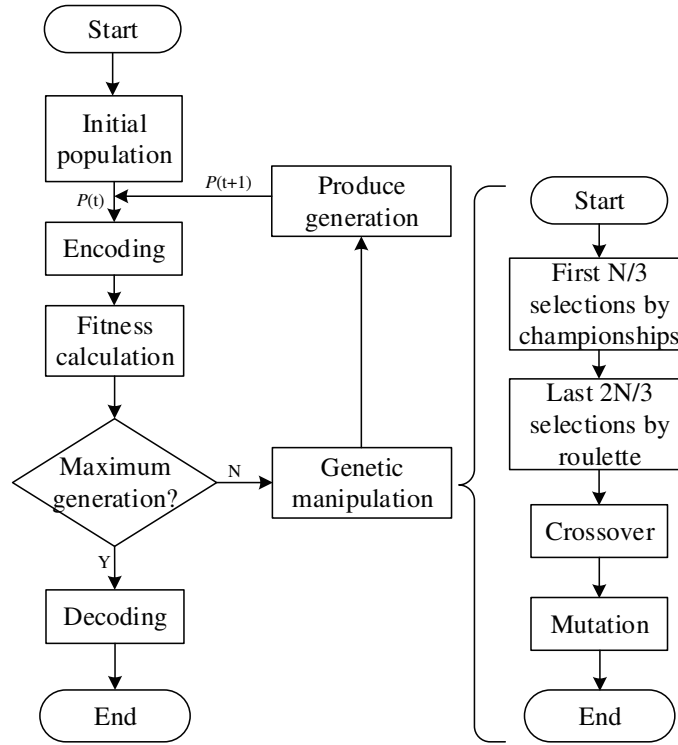


Figure 4. Flowchart of improved genetic algorithm.

To make the architecture of the proposed method more understandable, the overall IGA procedure can be divided into five steps below.

Step 1: The population size is set to 20, and the population is initialized. The selection range of k_p is (2000, 3000), and the selection range of k_d is (0, 200). To obtain the parameters as accurate as possible, iterations number is set to 300 generations.

Step 2: To get a good dynamic characteristics as well as a good transition process, Integral Time Absolute Error (ITAE) is used as the objective function of parameter selection:

$$J = \int_0^T t |e(t)| dt \quad (12)$$

where T is the simulation time, and $e(t)$ is the displacement error of the rotor.

Because the selection of the parameters means to search the minimum number of the objective function, the inverse of the objective function needs to be calculated:

$$f = \frac{1}{J} \quad (13)$$

Step 3: After the fitness of each individual is obtained, if the maximum genetic algebra is not reached, the selection operation is performed according to the fitness.

As can be seen in Fig. 5, in the selection operation, the joint algorithm of championship method and roulette method is adopted. In the first $N/3$ iterations, the championship method is adopted first, and multiple samples are randomly selected each time, so that the optimal fitness individuals obtained in the early stage of the algorithm are directly saved, and the search ability of the algorithm in the first $N/3$ iterations is improved. In the last $2N/3$ iterations, the roulette method is used to inherit the individuals with high fitness to the next generation of population, which can effectively avoid the precocious and stagnation problems in the later stage of the algorithm.

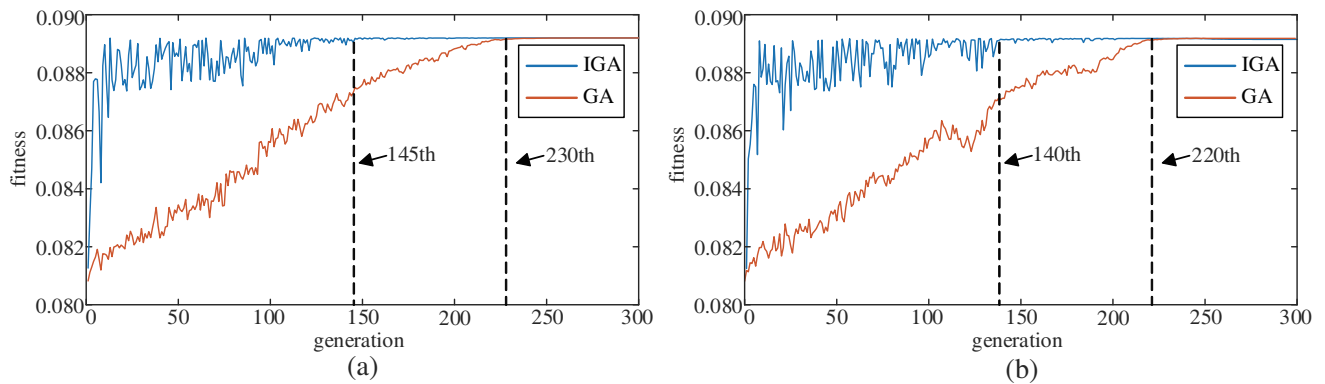


Figure 5. Fitness function curve comparison. (a) The optimization process of parameter k_p . (b) The optimization process of parameter k_d .

Step 4: After the improved selection operation in step 3, the next generation of chromosome is generated after crossover and mutation, and a new round of iteration process begins.

Step 5: All the above steps are repeated until the maximum number of iterations is obtained.

As can be seen in Fig. 5, The curves comparisons of the GA and IGA genetic generation with the fitness values are shown in Fig. 5. With the number of the iterations increasing, IGA converges faster than GA. In the first 100 iterations, by using the championship selection operation, the selection of the best fitness individual enters the next generation population, and the global search speed for the whole improved genetic algorithm is greatly accelerated. However, the search error of the tournament selection operation is large, so in the last 200 iterations, the roulette selection operation is used to approach the maximum with the advantage of the high precision. The best parameter k_p is obtained by GA at the 230th generation, and the best parameter k_d is obtained by GA at the 220th generation. After using the improved selection operation, the fitness rose rapidly throughout the genetic iteration. The best parameter k_p is obtained by IGA at the 145th generation, and the best parameter k_d is obtained by GA at the 140th generation. Compared with the GA and IGA, the search speed and fitting accuracy of optimal parameters by IGA have been greatly improved.

4. SIMULATION TEST

4.1. Simulation Experiment of Rotor Floating of Six-Pole Radial AMB

The simulation experiment of x direction rotor floating is shown in Fig. 6, and the displacement waveform in the y direction is identical to the x direction. The initial displacement setting of the six-pole radial AMB rotor is about 0.7 mm. Under the PID control, the time that the rotor returns to the equilibrium

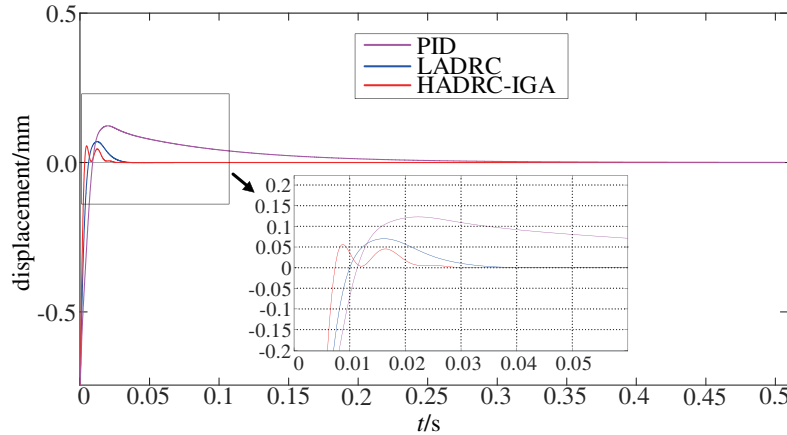


Figure 6. Simulation experiment of x direction rotor floating.

position is approximately 0.3 s, and the maximum deviation is about 0.13 mm; under the LADRC control, the time that the rotor returns to the equilibrium position is approximately 0.035 s, and the maximum deviation is about 0.07 mm; under the control of HADRC-IGA, the time that the rotor returns to the equilibrium position is approximately 0.025 s, and the maximum deviation is about 0.05 mm. The response time of HADRC-IGA is about 75% of LADRC, and the overshoot is about 71.4% of LADRC. Under the control of the HADRC-IGA, the response speed of the system is faster, and the overshoot is smaller.

4.2. Simulation Experiment of Rotor Anti-Interference and Decoupling of Six-Pole Radial AMB

The anti-interference curves for six-pole radial AMB under the control of the PID, LADRC, and HADRC-IGA in the x - and y -directions are shown in Fig. 7.

When the rotor is stably suspended, an interference force is applied to the rotor at 0.59 s and 0.63 s in the x direction, and the applied interference force is 50 N and 60 N respectively at 0.59 s and 0.63 s. According to Fig. 7(a), when the interference is applied at 0.59 s, the displacement of the rotor in the x direction is 0.13 mm, and the displacement of the rotor in the y direction is 0.12 mm. When the interference is applied at 0.63 s, the displacement of the rotor in the x direction is 0.15 mm, and the displacement of the rotor in the y direction is 0.13 mm. The time that the rotor returns to the equilibrium position is approximately 0.03 s. In Fig. 7(b), when the interference is applied at 0.59 s, the displacement of the rotor in the x - and y -directions is 0.08 mm and 0.06 mm, respectively. When the interference is applied at 0.63 s, the displacement of the rotor in the x - and y -directions is 0.09 mm and 0.06 mm, respectively. The time that the rotor returns to the equilibrium position is approximately 0.02 s. In Fig. 7(c), when the interference is applied at 0.59 s, the displacement of the rotor in the x - and y -directions is 0.04 mm and 0.01 mm, respectively. When the interference is applied at 0.63 s, the displacement of the rotor in the x - and y -directions is 0.05 mm and 0.01 mm, respectively. The time that the rotor returns to the equilibrium position is approximately 0.02 s. According to the simulation results, under the control of HADRC-IGA, the recovery time is 50% of LADRC, and the coupling amount is 12.5% of LADRC. When different interference forces are applied in a short time, the rotor can quickly return to the balance position under the control of HADRC-IGA; the response speed of the system is faster; the coupling is smaller; and the anti-interference ability is stronger.

5. EXPERIMENT RESEARCH

5.1. Experimental Platform and Sample Data Acquisition

The main parameters of the six-pole radial AMB in this paper are given in Table 1.

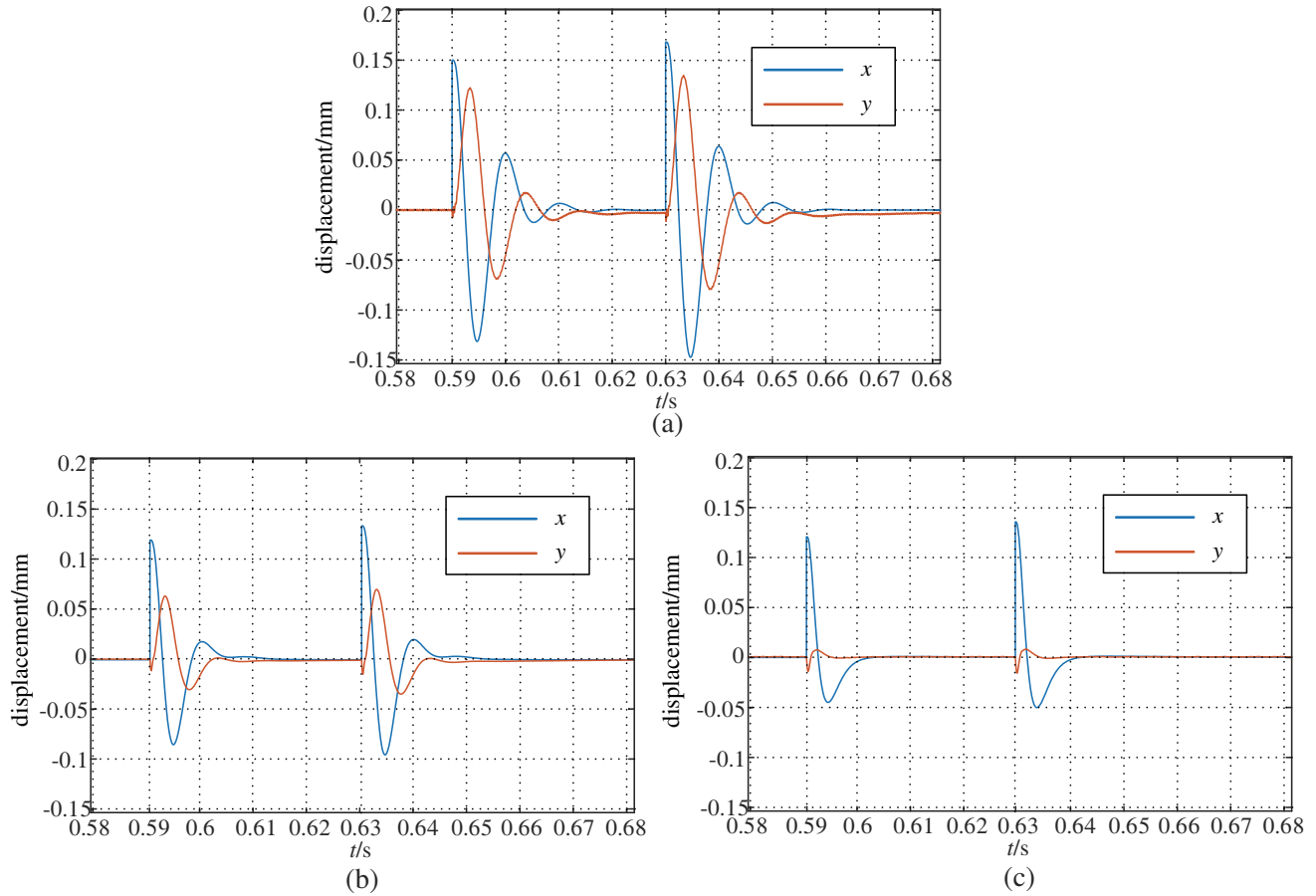


Figure 7. Simulation experiment of rotor anti-interference and decoupling. (a) Anti-interference and decoupling under PID. (b) Anti-interference and decoupling under LADRC. (c) Anti-interference and decoupling under HADRC-IGA.

The experimental platform of six-pole radial AMB to verify the above simulation results is shown in Fig. 8. The experimental platform mainly includes six-pole radial AMB, eddy current sensors, displacement interface circuit, digital signal processor (DSP), power amplifier circuit board, oscilloscope (OSC), PC, etc. The rotor floating experiment and the rotor anti-interference and decoupling experiment are performed by using the experimental platform.

In this paper, the CCS3.3 software developed for DSP provides an integrated environment for the software development of this system, in which the writing, debugging, and operation of the six-pole

Table 1. Main parameters of six-pole radial active magnetic bearing.

Parameters	Value
Saturation induction density B_s	0.8 T
Radial air gap length δ_0	0.5 mm
Magnetic pole area S_r	393 mm ²
Radial length of magnetic pole	23 mm
Axial length of magnetic pole	28 mm
Outer diameter of rotor	32 mm
Inner diameter of rotor	16 mm

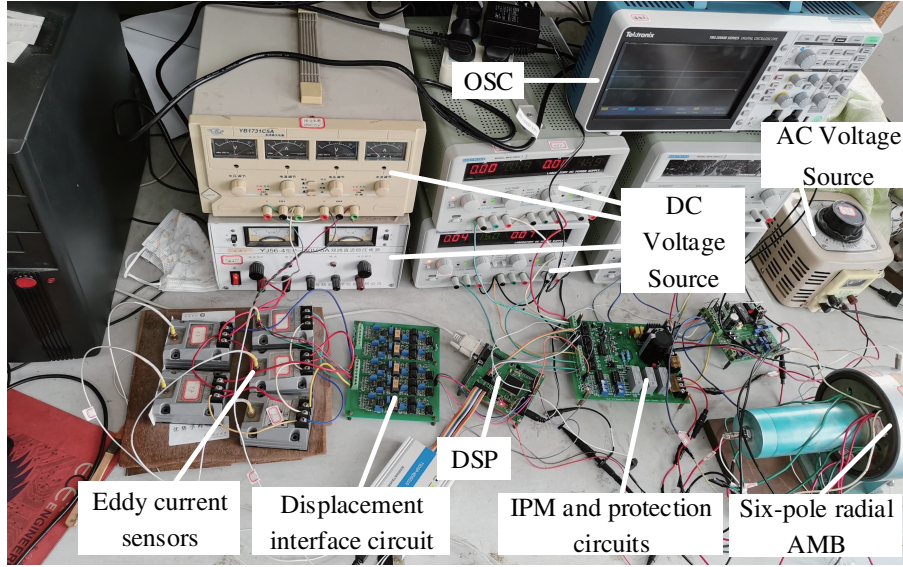


Figure 8. Experiment platform.

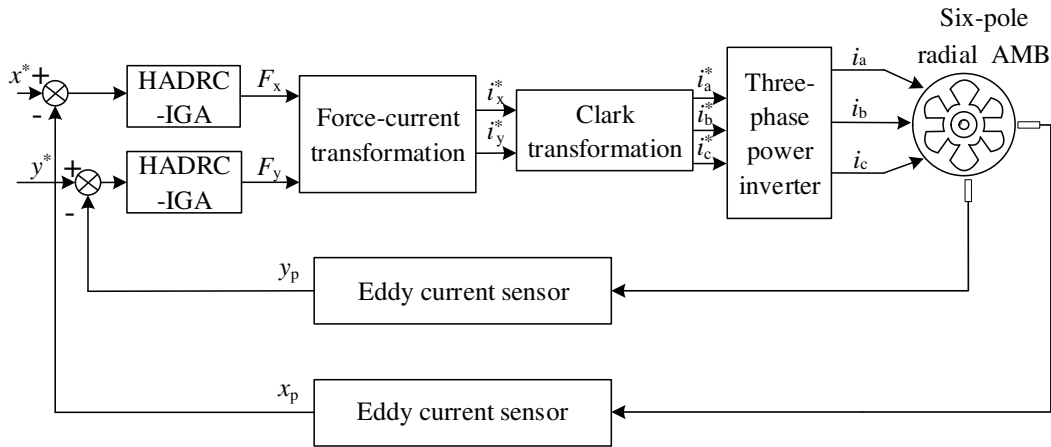


Figure 9. Sample acquisition experimental structure diagram.

AMB are completed. The man-machine interaction function realized by VB6.0 is mainly the real-time expression of the rotor suspension state of the magnetic bearing system and the online adjustment of the control parameters.

The control structure diagram is shown in Fig. 9. The eddy current displacement sensor outputs the detected displacement signals x_p and y_p as voltage signals, then the displacement interface circuit adjusts the amplitude of the voltage signal to the range within which the DSP can analyse. The DSP calculation generates 6-way PWM waves as the input to the three-phase power drive circuit for drive control, and there will be three-phase control currents i_a , i_b , and i_c in the three-phase coil. The control currents i_a , i_b , and i_c regulate the position offset of the rotor.

5.2. Experimental Verification

The waveform of the six-pole radial AMB rotor float experiment is shown in Fig. 10. As can be seen from Fig. 10(a), Fig. 10(b), and Fig. 10(c), when the system is controlled by the PID, the rotor returns to the equilibrium position after about 120 ms; when the system is controlled by the LADRC, the rotor returns to the equilibrium position after about 70 ms; and when the system is controlled by the HADRC-IGA,

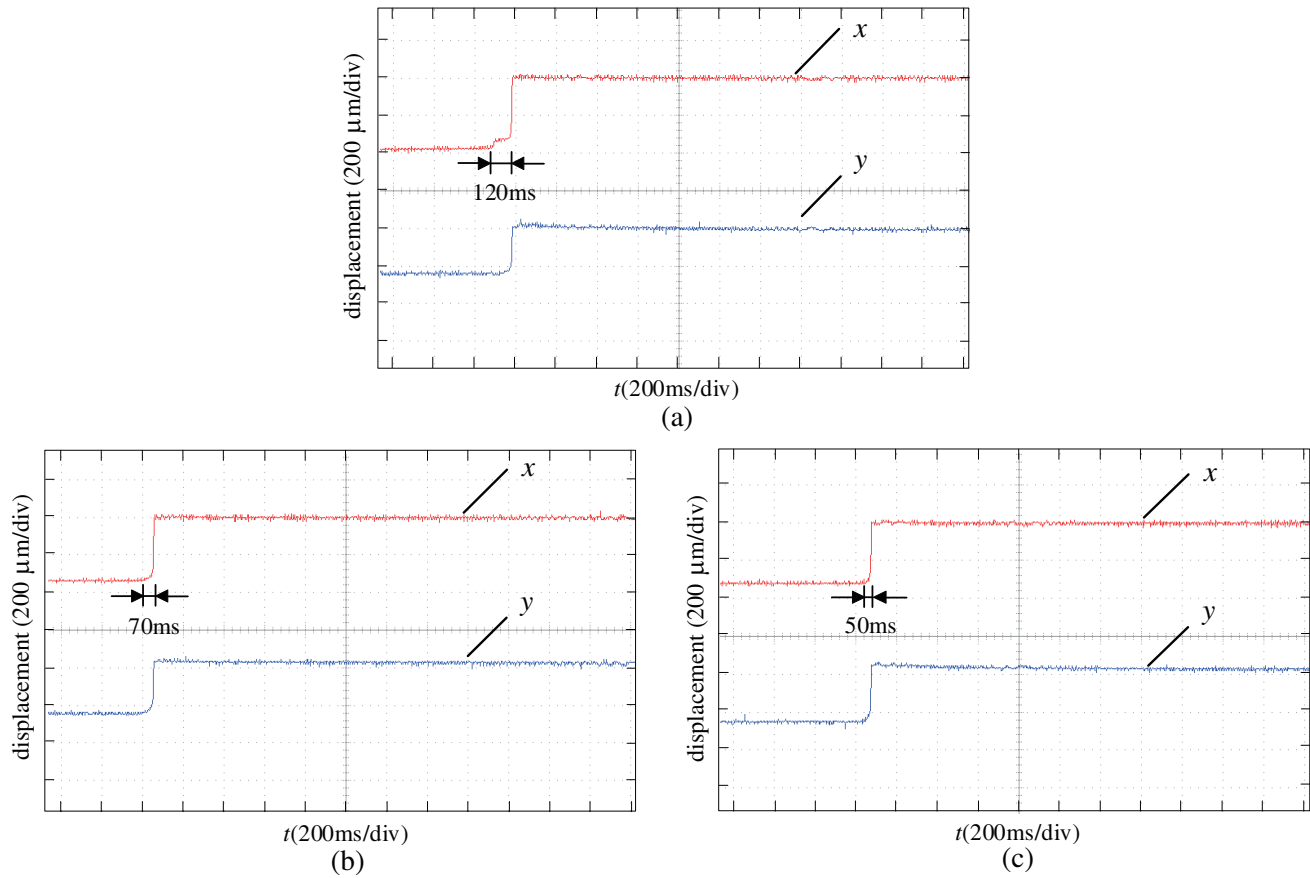
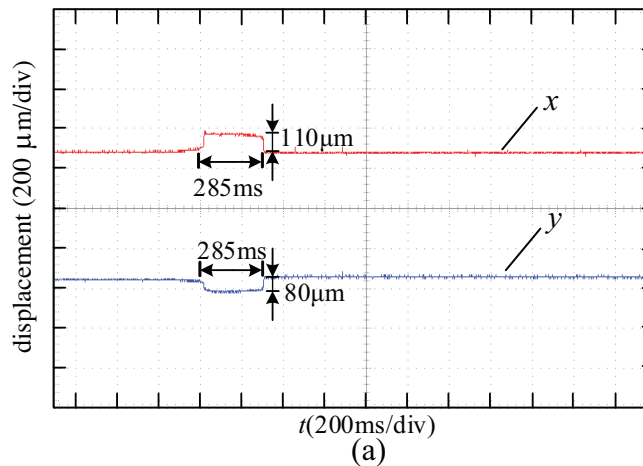


Figure 10. The waveform of the six-pole radial AMB rotor floating. (a) Rotor floating under PID. (b) Rotor floating under LADRC. (c) Rotor floating under HADRC-IGA.

the rotor returns to the equilibrium position after about 50 ms. The experimental result shows that under the control of HADRC-IGA, the speed of the rotor returning to the equilibrium position increases by 58.3% compared with that under the control of the PID. The six-pole radial AMB has better floating performance under the control of HADRC-IGA.

The displacement of the rotor when an external force of 150 N is applied in the x direction under the control of the PID, LADRC, and HADRC-IGA is shown in Fig. 11.

Figure 11 shows the experimental diagram of the six-pole radial AMB rotor loading. When the



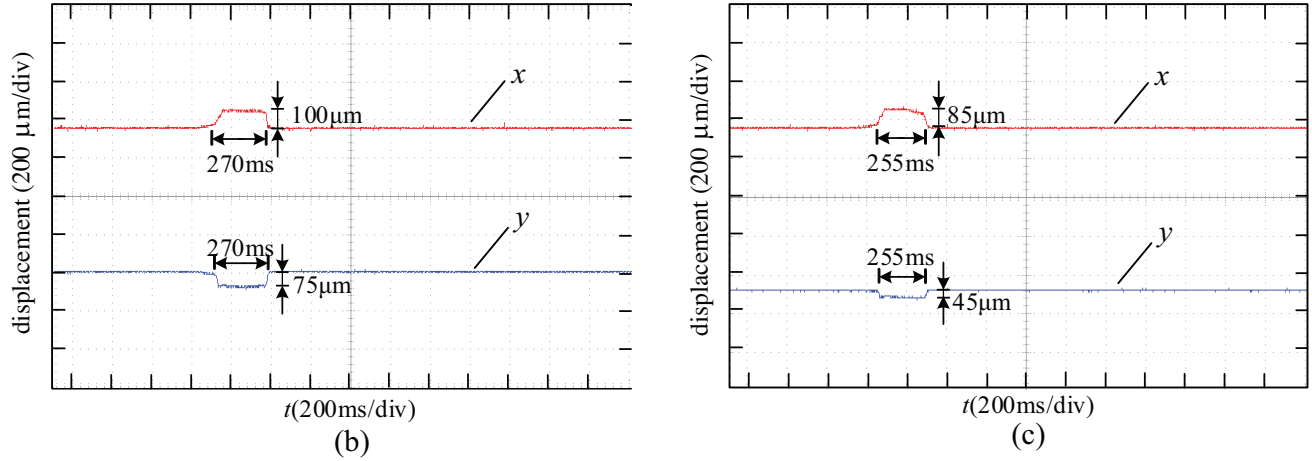


Figure 11. The waveform of load on six-pole radial AMB. (a) Anti-interference and decoupling under PID. (b) Anti-interference and decoupling under LADRC. (c) Anti-interference and decoupling under HADRC-IGA.

rotor is stably suspended, a 150 N weight is suspended in the x direction under the PID control. After applying the load, the deviation of the rotor from the equilibrium position is about $110\ \mu\text{m}$ and $80\ \mu\text{m}$ in the x - and y -directions, respectively, and the rotor returns to the equilibrium position after 285 ms. Under the control of the LADRC, the deviation of the rotor from the equilibrium position is about $100\ \mu\text{m}$ and $75\ \mu\text{m}$ in the x - and y -directions, respectively, and the rotor returns to the equilibrium position after 270 ms. Under the control of the HADRC-IGA, the time for the rotor to return to the equilibrium position is reduced to 255 ms, and the deviation of the rotor from the equilibrium position in the x - and y -directions is reduced to $85\ \mu\text{m}$ and $45\ \mu\text{m}$, respectively. The three experimental results show that under the control of the HADRC-IGA, if one direction of the six-pole radial AMB is subjected to an external force, the interference to the other direction is smaller, and the decoupling effect is better.

6. CONCLUSION

In this paper, the hybrid active disturbance rejection control based on improved genetic algorithm (HADRC-IGA) is applied to the six-pole radial AMB. The effectiveness of the controller is verified by simulation and experiment, and the following conclusions are obtained:

- (1) The linear active disturbance rejection control strategy of model compensation is proposed. Only ω and ω_c need to be determined by the strategy. The difficulty of parameter setting of the linear active disturbance rejection controller is greatly reduced.
- (2) The proposed HADRC-IGA has a strong robustness against disturbance and can effectively inhibit the displacement change of the six-pole radial AMB rotor system during the application of disturbance. After the HADRC-IGA is applied to the six-pole radial AMB, the coupling between the rotor displacements can be basically eliminated; the response speed of the system to the disturbance can be significantly improved; and the anti-interference ability of the six-pole radial active magnetic bearing is stronger.

ACKNOWLEDGMENT

This project was sponsored in part by the National Natural Science Foundation of China (61973144, 62273168).

REFERENCES

1. Liu, Y. F., M. Y. Huo, and N. M. Qi, "Modeling of disturbance torque in an aerostatic bearings-based nano-satellite simulator," *Journal of Systems Engineering and Electronics*, Vol. 29, No. 3, 618–624, June 2018.
2. Wang, Y., Q. Zhang, L. Zhao, and E. S. Kim, "Non-resonant, broad-band vibration-energy harvester based on self-assembled liquid bearing," *2015 Transducers- 2015 18th International Conference on Solid-State Sensors, Actuators and Microsystems (TRANSDUCERS)*, 614–617, 2015.
3. Le, Y., J. Sun, and B. Han, "Modeling and Design of 3-DOF magnetic bearing for high-speed motor including eddy-current effects and leakage effects," *IEEE Trans. Ind. Electron*, Vol. 63, No. 6, 3656–3665, June 2016.
4. Gupta, S., J. Laldingliana, S. Debnath, and P. K. Biswas, "Closed loop control of active magnetic bearing using PID controller," *2018 International Conference on Computing, Power and Communication Technologies (GUCON)*, 686–690, 2018.
5. Chen, S.-L., S.-Y. Lin, and C.-S. Toh, "Adaptive unbalance compensation for a three-pole active magnetic bearing system," *IEEE Trans. Ind. Electron*, Vol. 67, No. 3, 2097–2106, March 2020.
6. Chen, S.-L. and S.-Y. Lin, "Adaptive imbalance compensation for a three-pole AMB system," *2016 12th IEEE International Conference on Control and Automation (ICCA)*, 962–965, 2016.
7. Jin, Z., X. Sun, L. Chen, and Z. Yang, "Robust multi-objective optimization of a 3-pole active magnetic bearing based on combined curves with climbing algorithm," *IEEE Trans. Ind. Electron*, Vol. 69, No. 6, 5491–5501, June 2022.
8. Jiang, K. J., C. S. Zhu, and L. L. Chen, "Unbalance compensation by recursive seeking unbalance mass position in active magnetic bearing-rotor system," *IEEE Trans. Ind. Electron*, Vol. 62, No. 9, 5655–5664, September 2015.
9. Wang, S. S., H. Q. Zhu, M. Y. Wu, and W. Y. Zhang, "Active disturbance rejection decoupling control for three-degree-of- freedom six-pole active magnetic bearing based on BP neural network," *IEEE Transactions on Applied Superconductivity*, Vol. 30, No. 4, 1–5, June 2020.
10. Tang, J. Q., K. Wang, and B. Xiang, "Stable control of high-speed rotor suspended by superconducting magnetic bearings and active magnetic bearings," *IEEE Trans. Ind. Electron*, Vol. 64, No. 4, 3319–3328, April 2017.
11. Peng, C., J. Sun, C. X. Miao, and J. C. Fang, "A novel cross-feedback notch filter for synchronous vibration suppression of an MSFW with significant gyroscopic effects," *IEEE Trans Ind Electron*, Vol. 64, No. 9, 7181–7190, September 2017.
12. Yu, Y. J., X. D. Sun, and W. Y. Zhang, "Modeling and decoupling control for rotor system in magnetic levitation wind turbine," *IEEE Access*, Vol. 5, 15516–15528, 2017.
13. Wang, D. and H. Sun, "Design of repetitive controller based on linear auto disturbance rejection control for active magnetic bearing spindles," *2017 2nd International Conference on Cybernetics, Robotics and Control (CRC)*, 106–110, 2017.
14. Ren, G. P., Z. Yu, Y. Wu, S. Chen, X. Li, and H. T. Zhang, "The analysis of similarities and differences between ADRC and PID controller for AMB system," *2021 40th Chinese Control Conference (CCC)*, 274–279, 2021.
15. Lu, Y. Y. and P. L. Wu, "Design of turret servo system based on optimized model-compensation active disturbance rejection controller," *2019 International Conference on Control, Automation and Information Sciences (ICCAIS)*, 1–6, 2019.
16. Gao, Z. Q., "Scaling and bandwidth-parameterization based controller tuning," *Proceedings of the 2003 American Control Conference*, 4989–4996, 2003.
17. Li, X., et al., "A decoupling synchronous control method of two motors for large optical telescope," *IEEE Trans. Ind. Electron*, Vol. 69, No. 12, 13405–13416, December 2022.